JGR Space Physics

RESEARCH ARTICLE
10.1029/2019JA027708

Millstone Hill ISR Measurements of Small Aspect Angle Spectra

William J. Longley[1,2,3], Philip J. Erickson[4], Juha Vierinen[5], Meers M. Oppenheim[1], Frank D. Lind[4], and Yakov S. Dimant[1]

[1]Center for Space Physics, Boston University, Boston, MA, USA, [2]Department of Physics and Astronomy, Rice University, Houston, TX, USA, [3]University Corporation for Atmospheric Research, Boulder, CO, USA, [4]Haystack Observatory, Massachusetts Institute of Technology, Westford, MA, USA, [5]Department of Physics and Technology, University of Tromsø, Tromsø, Norway

Key Points:
- Millstone Hill measured incoherent scatter spectra at small aspect angles to test different models of determining ionospheric temperatures
- Collisions narrowed measured spectra at aspect angles less than 4.6° for high densities, and at angles less than 1.25° for low densities
- A nonlinear particle-in-cell forward model is shown to produce larger, more realistic, T_e/T_i estimates than current forward models

Correspondence to:
W. J. Longley,
wlongley@rice.edu

Citation:
Longley, W. J., Erickson, P. J., Vierinen, J., Oppenheim, M. M., Lind, F. D., & Dimant, Y. S. (2020). Millstone Hill ISR measurements of small aspect angle spectra. *Journal of Geophysical Research: Space Physics*, *124*, e2019JA027708. https://doi.org/10.1029/2019JA027708

Received 6 DEC 2019
Accepted 17 APR 2020
Accepted article online 4 MAY 2020

Abstract The Millstone Hill incoherent scatter (IS) radar is used to measure spectra close to perpendicular to the Earth's magnetic field, and the data are fit to three different forward models to estimate ionospheric temperatures. IS spectra measured close to perpendicular to the magnetic field are heavily influenced by Coulomb collisions, and the temperature estimates are sensitive to the collision operator used in the forward model. The standard theoretical model for IS radar spectra treats Coulomb collisions as a velocity independent Brownian motion process. This gives estimates of $T_e/T_i < 1$ when fitting the measured spectra for aspect angles up to 3.6°, which is a physically unrealistic result. The numerical forward model from Milla and Kudeki (2011, https://doi.org/10.1109/TGRS.2010.2057253) incorporates single-particle simulations of velocity-dependent Coulomb collisions into a linear framework, and when applied to the Millstone data, it predicts the same T_e/T_i ratios as the Brownian theory. The new approach is a nonlinear particle-in-cell (PIC) code that includes velocity-dependent Coulomb collisions which produce significantly more collisional and nonlinear Landau damping of the measured ion-acoustic wave than the other forward models. When applied to the radar data, the increased damping in the PIC simulations will result in more physically realistic estimates of T_e/T_i. This new approach has the greatest impact for the largest measured ionospheric densities and the lowest radar frequencies. The new approach should enable IS radars to obtain accurate measurements of plasma temperatures at times and locations where they currently cannot.

1. Incoherent Scatter at Small Aspect Angles

Incoherent scatter (IS) radars measure the plasma temperature, density, and ion drift velocity in the ionosphere over a large range of altitudes, local times, seasons, and geomagnetic conditions. The decades of data produced by these radars are heavily utilized by researchers, including studies of short-term phenomena such as plasma drifts and the onset of Equatorial Spread-F (Beynon & Williams, 1978; Evans, 1972; Hysell et al., 2015), system scale magnetosphere-ionosphere coupling phenomena (Foster et al., 2002), and long-term solar cycle studies through assimilation into models such as IRI and MSIS (Bilitza & Reinisch, 2008; Hedin, 1991). While these data sets are generally robust, the electron and ion temperatures are known to be systematically underestimated when the radar line of sight is nearly perpendicular to the Earth's magnetic field. Aponte et al. (2001) gives a thorough review on the discovery and history of this "perpendicular to B" problem at the equatorially located Jicamarca Radio Observatory. This same perpendicular to B problem is also present at the Millstone Hill IS radar for azimuthal scans at low elevation angles in the north and west directions and for the ALTAIR IS radar. In this work, we use the 440-MHz midlatitude Millstone Hill IS radar to measure small aspect angle spectra and then compare the spectra to three different models for IS spectra: nonlinear PIC simulations from Longley et al. (2019), linear single-particle simulations from Milla and Kudeki (2011), and a linear Brownian collisional theory (Kudeki & Milla, 2011).

The IS radar technique estimates temperatures by fitting a forward model of the heavily Landau damped ion-acoustic plasma resonance mode to the Doppler spectra measured by the radar. This fitting process is often done to the autocorrelation function (ACF) of the radar (calculated from the measured backscatter electric field), which is the Fourier transform of the Doppler spectra into the time domain. At magnetic aspect angles less than 5° from perpendicular to B, the ion-acoustic mode gains an additional source of damping as the

magnetic field constrains electron motion in response to the wave's electric field. At these small aspect angles, an electron has to move a longer distance along B in order to move one wavelength towards or away from the radar, and this increased transit time gives a higher probability that the electron will collide with another electron or an ion, thus changing its trajectory and contributing more damping to the acoustic mode. Sulzer and González (1999) showed that this physical picture adds an additional damping source to the ion-acoustic mode at small aspect angles, which previous IS radar theory neglected. The resulting collisional narrowing of the spectra has a similar effect on IS radar spectra as an increase in the Landau damping. Landau damping is increased for smaller T_e/T_i ratios (Froula et al., 2011), so fitting collisionless forward models to the collisionally narrowed spectra underestimates the T_e/T_i ratio and can even calculate nonphysical $T_e/T_i < 1$ ratios, which is the end effect of the "perpendicular to B" problem.

Sulzer & González, 1999 showed that Coulomb collisions are responsible for the temperature underestimates by developing a forward model of IS radar spectra that includes electron–ion and electron–electron collisions. The Sulzer and Gonzalez model calculates IS radar spectra by simulating the trajectory of a single electron subjected to collisional and magnetic forces, with the method later extended to aspect angles smaller than 0.1° by Milla and Kudeki (2011). The Sulzer and Gonzalez model was compared to data from the 50-MHz Jicamarca IS radar in Aponte et al. (2001), showing that nonphysical $T_e/T_i < 1$ ratios measured at small aspect angles could be corrected to physically valid values. However, fully kinetic particle-in-cell (PIC) simulations from Longley et al. (2018, 2019) showed that previously neglected kinetic effects from electron–electron collisions cause a further narrowing of the small aspect angle spectra compared to the single-particle simulations of Sulzer and González (1999) and Milla and Kudeki (2011) or to the collisional theories developed in Woodman (2004) and Kudeki and Milla (2011). This paper seeks to understand the results of Longley et al. (2018, 2019) by comparing spectra from the PIC simulations to the single-particle simulations, which are in turn compared to spectra measured at Millstone Hill.

It is useful to summarize the experiments that Aponte et al. (2001) analyzed with the 50-MHz Jicamarca radar to validate the single-particle model from Sulzer and González (1999). The first experiment occurred an hour after sunset and looked at aspect angles between 2° and 2.25° and altitudes of 330 to 550 km. Fitting the measured ACFs from this experiment to collisionless IS radar theory found nonphysical $T_e/T_i < 1$ ratios at all altitudes, while refitting the ACFs to the collisional single-particle simulations of Sulzer and González (1999) produced $T_e/T_i \approx 1$ as expected at night. The same aspect angles were probed during the afternoon at altitudes of 200 to 550 km and showed that the T_e/T_i ratio from collisionless theory was significantly less than the ratio obtained by fitting to single-particle simulations. The next experiment analyzed aspect angles between 3° and 3.5° from 330 to 550 km in altitude at night. At this pointing direction, the same results were found: T_e/T_i was less than 1 when fit to collisionless theory, while fitting to single-particle simulations found $T_e/T_i \approx 1$ as expected. The last experiment analyzed by Aponte et al. (2001) was a daytime measurement of aspect angles between 4.5° and 5° at altitudes of 200 to 500 km. For these aspect angles, the difference in T_e/T_i between collisionless theory and single-particle simulations was minimal. In aggregate, therefore, Aponte et al. (2001) showed that fitting data to the collisional single-particle simulations of Sulzer & González, 1999 led to more accurate and more physical T_e/T_i ratios at nominal aspect angles of 2° and 3°, but no significant difference existed between the two forward models at aspect angles of 4.5° or larger. For this paper and the results of Aponte et al. (2001), it is important to understand that, barring rare satellite conjunctions, the only ground truth when fitting IS spectra during non-storm time conditions is that $T_e/T_i \geq 1$ during the day, and $T_e = T_i$ at night. This is due to photoionization preferentially heating electrons during the day and both species coming to equilibrium at night.

The goal of this paper is twofold. First, daytime spectra are measured at Millstone Hill and fit to the Brownian theory (Kudeki & Milla, 2011) and single-particle simulations (Milla & Kudeki, 2011) to see if these forward models predict that $T_e/T_i \geq 1$. These spectra are measured across a larger range of aspect angles than those in Aponte et al. (2001) and therefore show what range of aspect angles require an accurate collisional forward model. The second goal of this paper is to validate the PIC simulations from Longley et al. (2018, 2019) by directly comparing them to the Brownian theory and single-particle simulations for one set of T_e, T_i chosen from fits to the data. If the PIC simulations produce narrower spectra than either forward model, then the PIC simulations would produce a higher T_e/T_i if fit directly to the data. We do not directly fit the PIC simulations to the data as the computational cost of the PIC code is currently too high.

Table 1
Summary of the Different Experiments at Millstone Hill Used in This Study

Date	Range resolution	(Az., Elev.)	Integration time	Aspect angles	Ranges (km)	Figures
8 November 2013	15 km	(−12°, 4.4°)	15:20 to 16:43	0.25° to 5°	1,185 to 1,530	1, 4, and 7
22 February 2019	18 km	(−20°, 10°)	16:02 to 16:18	0.4° to 4.8°	840 to 1,152	2a and 5a–5c
		(−55°, 10°)	16:22 to 16:37	5.3° to 9.5°	840 to 1,152	2b and 5d–5f
		(−20°, 6°)	16:38 to 16:55	−0.05° to 4.7°	1,062 to 1,410	Not used
4 April 2019	18 km	(−12°, 8°)	15:36 to 15:53	−0.2° to 4.3°	942 to 1,266	3a and 6f
		(−12°, 15°)	15:55 to 16:32	2.2° to 5.9°	648 to 918	3b and 6a–6c
		(−12°, 12°)	16:44 to 17:15	0.8° to 4.9°	750 to 1,044	3c and 6d–6f
		(−12°, 45°)	17:29 to 17:39	25° to 27°	276 to 414	Not used

Note. For each listed date and pointing direction, the ACFs were integrated over the listed local times to reduce noise under the assumption of stable ionospheric conditions. The listed aspect angles and range to target are taken at altitudes of 200 km, where the O+ dominated F2 region is assumed to start and 300 km where SNR typically becomes too low for the elevation angles used. Data are available at Erickson (2013, 2019a, 2019b).

1.1. Experimental Setup

The Millstone Hill Observatory in Westford, Massachusetts, has a large aperture, high power UHF radar system used since 1960 for Thomson or IS remote sensing of the ionosphere (Gordon, 1958). The Millstone Hill system is composed of a megawatt class UHF transmitter at 440 MHz and two IS capable radar antennas: the 68-meter zenith pointing antenna and the fully steerable 46-meter MISA antenna. With the MISA antenna pointed in the general magnetic north direction, small magnetic aspect angles can be observed above 200 km in the O^+ dominated F_2 region. However, the range to these aspect angles of interest can be upwards of 1,400 km from the radar, and the resulting spectra can exhibit low signal-to-noise ratios. For this reason, a coded long pulse is employed to maintain high-range resolution at the aspect angles of interest while preserving the high SNR (large energy on target) of a long pulse envelope.

For the experiments reported here, two different pseudorandom pulse codes with 2-ms envelope length were implemented to obtain high-range and aspect angle resolution (Lehtinen & Häggström, 1987; Sulzer, 1986). The first experiment in November 2013 cycled between 32 different 100-baud pseudorandom codes, with the 20-μs baud length providing 3-km effective range resolution after decoding. To reduce noise, the ACFs were further averaged post-decode over five consecutive range gates, giving an effective range resolution of 15 km. The second set of experiments in February and April 2019 targeted improved SNR while maintaining high-range resolution and therefore cycled between 50 different 50-baud pseudorandom codes, with the baud length of 40 μs providing a post-decode range resolution of 6 km. Due to the lower F-region density during those solar minimum condition experiments, the ACFs were averaged post-decode across three range gates to improve the SNR, giving an effective range resolution of 18 km. The measured ACFs were deconvolved using the technique in Virtanen et al. (2008) to remove range ambiguities.

For this study, three different experiments using the two classes of codes described above were performed with the Millstone Hill MISA antenna. The first experiment (Erickson, 2013) occurred on 8 November 2013 with the antenna pointed at −12° azimuth and 4.4° elevation. The ACFs were obtained using the 100-baud code with 15-km range resolution and were integrated from 15:20 to 16:43 local time under stable ionospheric conditions. The second experiment (Erickson, 2019a) took place on 22 February 2019, and three sets of data were collected between 16:00 and 17:00 local time at different pointing positions with 18-km range resolution. The last experiment (Erickson, 2019b) occurred on 4 April 2019 between 15:30 and 17:40 local daylight savings time using the same 50-baud code as the February 2019 experiment. Table 1 summarizes all of the experiments at Millstone Hill.

2. IS Radar Temperature Retrieval

2.1. Forward Models

The IS radar remote sensing technique measures electron and ion temperatures through an inversion process where a forward model is fit to the data through a nonlinear least squares technique. The ACFs measured by Millstone Hill are compared to three forward models: Brownian collisional theory, single-particle simulations, and PIC simulations. The Brownian theory and single-particle simulations both use the linear framework in Kudeki and Milla (2011) to calculate the IS radar spectra. This framework uses the fluctuation-

dissipation theorem (e.g., Kubo, 1966) to relate the positional ACFs, $\left\langle e^{i\vec{k}\cdot\Delta\vec{r}}\right\rangle$, to the IS radar spectra, $\langle|n_e(\omega,k)|^2\rangle$, as (Kudeki & Milla, 2011)

$$<|n_e(\omega,k)|^2>=\left|\frac{i\omega\epsilon_0+\sigma_i}{i\omega\epsilon_0+\sigma_e+\sigma_i}\right|^2<|n_{te}|^2>+\left|\frac{\sigma_e}{i\omega\epsilon_0+\sigma_e+\sigma_i}\right|^2<|n_{ti}|^2>. \quad (1)$$

The conductivities, σ_s, and thermal scattering terms, $\langle|n_{ts}|^2\rangle$ are

$$\sigma_s\left(\omega,\vec{k}\right)=\frac{i\omega\epsilon_0}{k^2h_d^2}(1-i\omega J_s), \quad (2)$$

$$<\left|n_{ts}\left(\omega,\vec{k}\right)\right|^2>=2N_0\mathrm{Re}[J_s], \quad (3)$$

where h_d is the Debye length for the species s and N_0 is the plasma density. The Gordeyev integral J_s (Gordeyev, 1952) is the one-sided Fourier transform of the positional ACF (Milla & Kudeki, 2011):

$$J_s\left(\omega,\vec{k}\right)=\int_0^\infty d\tau e^{-i\omega\tau}\left\langle e^{i\vec{k}\cdot\Delta\vec{r}}\right\rangle. \quad (4)$$

Equations 1–4 define the IS radar spectra once the ACF of each species is known. For a magnetized plasma, with collisions approximated as a Brownian motion process, the positional ACF is (Woodman, 1967; see also Kudeki & Milla, 2011)

$$<e^{i\vec{k}\cdot\Delta\vec{r}}>=\exp\left[-k_\parallel^2\frac{c_s^2}{\nu_{cs}^2}(\nu_{cs}\tau-1+e^{-\nu_{cs}\tau})\right]\times\exp\left[-k_\perp^2\frac{c_s^2}{\nu_{cs}^2+\Omega_s^2}(\cos(2\gamma)+\nu_{cs}\tau-e^{-\nu_{cs}\tau}\cos(\Omega_s\tau-2\gamma))\right]. \quad (5)$$

The first term describes how a given particle moves away from its initial position along B, over a time lag τ, while colliding at a constant collision rate ν_{cs}. The second term describes both the gyration around a magnetic field line and the collisional diffusion perpendicular to B. The parameter in the cosine functions is $\gamma\equiv\arctan(\nu_{cs}/\Omega_s)$. This Brownian theory is currently the most sophisticated analytic solution for collisional, magnetized IS radar spectra. However, the single-particle simulations in Milla and Kudeki (2011) and the PIC simulations in Longley et al. (2018, 2019) all show that the Brownian theory is not an accurate forward model for plasma temperature retrieval at small aspect angles.

To improve on the Brownian theory, Milla and Kudeki (2011) extended the single-particle simulation method first presented in Sulzer and González (1999). This forward model uses the same linear framework in equation 1–4 but calculates the positional ACFs numerically by simulating the motion of a particle subject to magnetic and collisional forces. The single-particle simulations use a Fokker-Planck collision operator for both electron–ion and electron–electron collisions. In these simulations electron–ion collisions significantly damp the ion-acoustic mode, which narrows the spectra more than predicted by the Brownian theory, whereas the electron–electron collisions are well modeled by a Brownian collision operator and primarily serve to stabilize the simulation (Longley et al., 2019). The most recent forward model to compare the measured spectra with is the PIC simulations from Longley et al. (2018, 2019). PIC codes simulate the trajectory of ~10^9 individual particles and calculate the density on a grid at every time step to solve Poisson's equation for a self-consistent electric field. The density is then Fourier transformed to directly calculate the IS spectra without needing the linear framework in equations 1–4. The PIC simulations use the same Fokker-Planck collision operators for electron–ion and electron–electron collisions as the single-particle simulations.

2.2. Inversion Methods

The analytic Brownian theory has the advantage of being fast to compute and therefore can be used for efficient fitting of measured data. Radars measure a voltage time series at the receiver terminals, which is a measure of the scattered electric field that is directly related to the medium's electron density fluctuations. The time series is then used to calculate the ACF of the density fluctuations, $<\left|n_e\left(\tau,\vec{k}\right)\right|^2>\equiv\left\langle n_e^*\left(t,\vec{k}\right)n_e\left(t+\tau,\vec{k}\right)\right\rangle$, or the corresponding Doppler spectra, $<\left|n_e\left(\omega,\vec{k}\right)\right|^2>$. Either the ACF or

spectra can be fitted to the Brownian forward model to estimate T_e and T_i. Fitting the ACF has the advantage of being able to weight each point in the time series according to how many measurements each lag in the ACF has. Once the ACF has been decoded, there are many weighting schemes that can be employed in the fitting process (Lehtinen & Huuskonen, 1996). We will use here the framework where a voltage signal at discrete time lags $\tau = 0,\Delta t,2\Delta t,...,N\Delta t$ is weighted at each time lag in the ACF as $W_\tau = \frac{1}{\sqrt{N}}, \frac{1}{\sqrt{N-1}}, \frac{1}{\sqrt{N-2}}, \ldots, 1$.

The ACF fitting is then accomplished using the nonlinear, least squares Levenberg-Marquardt algorithm to search (T_e, T_i) space while minimizing the cost function

$$\chi^2(T_e, T_i) = \sum_\tau \left(< |n_{\text{Theory}}(\tau,k)|^2 > - < |n_{\text{Data}}(\tau,k)|^2 > \right) \cdot W_\tau^2. \quad (6)$$

Note that the weights W_τ do not directly modify the measured ACF and are only used in the fitting process. For each fitted ACF, the error bars on T_e and T_i are computed as the 95% confidence interval using the Jacobian from the least squares routine.

The measured ACF depends on several plasma parameter values, not only on T_e and T_i but also on electron density and line of sight ion velocity. The 0th lag of the ACF, which measures the total power of the system, is dependent on the electron density and temperatures as $N_0/(1+T_e/T_i)$. To produce an electron density measurement, this total power therefore needs to be calibrated through the radar equation and corrected for the $1/(1+T_e/T_i)$ temperature scaling. Millstone Hill typically finds the calibration factor using either the plasma/Langmuir line frequency or the foF2 frequency from the on-site digital ionosonde run by the University of Massachusetts Lowell. Since the total power is calibrated separately and only effects the overall scaling of the ACF and spectra, it is not included in the fitting process. This is done by setting the weight of the 0th lag to $W_0 = 0$ and then normalizing the whole ACF by the value at the first nonzero time lag. The electron density is still needed however in the Brownian theory to calculate the collision rates, which scale as $\nu_e \propto N_0$, so a 0th-order density value taken from IRI is used as an approximation only for the collision rates. This does not introduce any significant errors when fitting ACFs at Millstone's wavelength since the Brownian theory becomes effectively collisionless at aspect angles larger than ~0.5° (Longley et al., 2019). Similarly, the line of sight ion velocity is excluded from the fitting process since it only affects the mean Doppler shift of the spectra, which is typically much smaller than the width of the spectra. The ion velocity is excluded from the fitting process by calculating the theory with $v_{\text{ion}} = 0$ and fitting only the real part of the measured ACF. The magnetic field near Millstone Hill varies from 0.505 G at 200 km to 0.48 G at 300 km, with a dependence on the altitude, latitude, and longitude. To simplify the fitting process, a constant magnetic field of 0.5 G is used for all of the fits in this paper. This primarily affects the ratio ν_{cs}/Ω_s, and thus collision rate, in the Brownian ACF from equation 5 since the electron motion remains tied to the field lines for the range of magnetic field values near Millstone.

Figures 1–3 show the measured spectra for the different experiments at Millstone Hill. In the next section, the temperatures and associated error bars for each fit are examined in detail. The data show a significant narrowing of the spectra at aspect angles below 1°, which indicates that the exactly perpendicular to B spectra is being measured within the main lobe of the antenna. This is because the spectral width decreases from ~7 kHz for unmagnetized spectra to ~200 Hz for perpendicular spectra, while maintaining a roughly constant total power (Milla & Kudeki, 2011). Fitting spectra at these aspect angles therefore requires an accurate averaging of the forward model across the ~1.2° beam width and from the front to back of each range gate. This beam averaging is not included in the fittings shown below, as the focus of this paper is on aspect angles between about 2° to 6° where the spectra starts converging to collisionless theory. The Brownian, single-particle, and PIC forward models all converge to collisionless theory at different aspect angles (Longley et al., 2019), and therefore, the convergence in the data is a direct way of validating the forward models. Furthermore, at aspect angles above 2°, the shape of the spectra changes slowly with aspect angle, and the beam averaging is less important.

3. Aspect Angles Where Collisions Matter

The simple Brownian collision theory allows for fast and efficient processing of data at large aspect angles where collisions do not narrow the spectra. Therefore, it is important to know the range of aspect angles where the Brownian theory is not appropriate for fitting measured spectra, and a better forward model

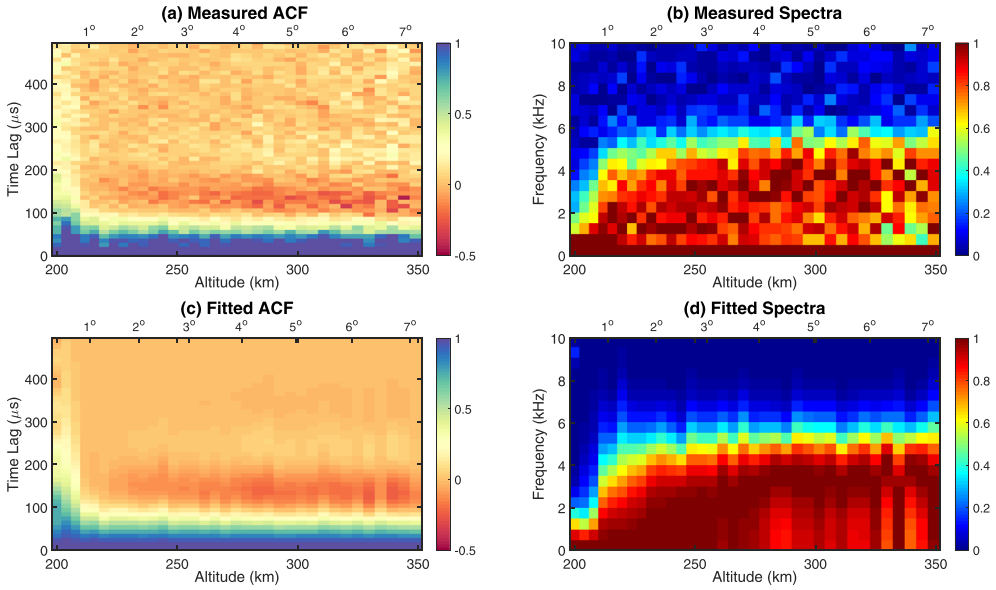

FIGURE 1. The normalized ACFs measured on 8 November 2013 are shown in plot (a). The ACFs are fit to the Brownian collisional model in plot (c). Plots (b) and (d) show the spectrograms corresponding to the data and fitted ACFs, respectively. The perpendicular to B region at ~200-km altitude corresponds to a broadening of the ACF (plots a and c) and a narrowing of the spectra (plots b and d). Figure 7 shows select ACFs and the fits to them.

needs to be used. Ideally, this range of aspect angles would be determined by comparing IS radar temperature estimates to temperatures measured by an independent method. Without having a spacecraft/in situ instrument as a reference, the next best indication of collisions affecting temperature estimates is obtaining nonphysical ratios of $T_e/T_i < 1$. We can use this as an effective indicator of theory-data divergence as the data collected in this paper were taken during the day, when photoionization should preferentially heat the electrons to a higher temperature than the ions.

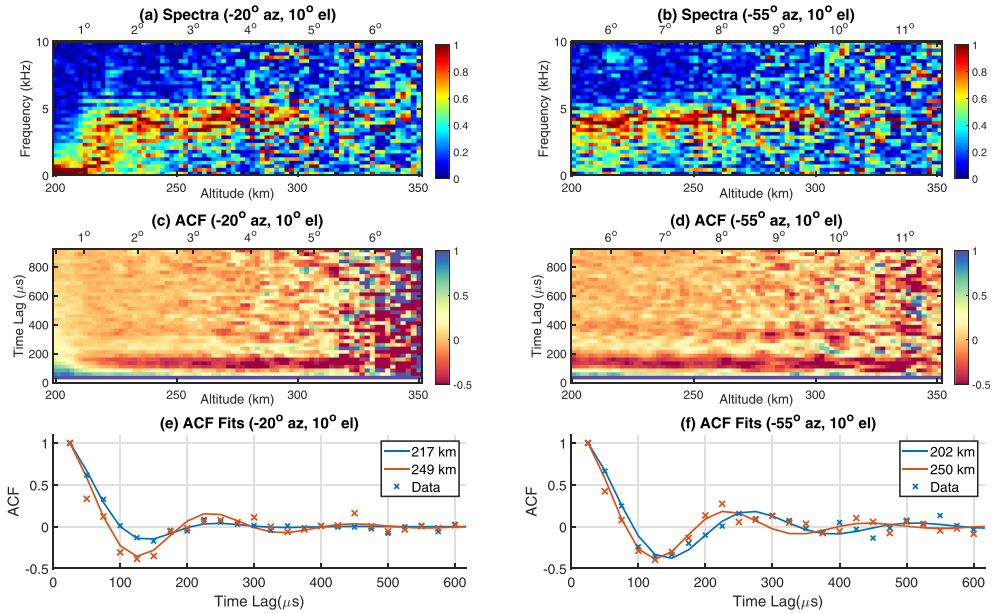

FIGURE 2. Spectrograms measured on 22 February 2019 are shown in plots (a) and (b). The ACFs in plots (c) and (d) are fit to the Brownian collisional model. Plots (e) and (f) show selected best fits (solid colors) to the measured ACFs (x points).

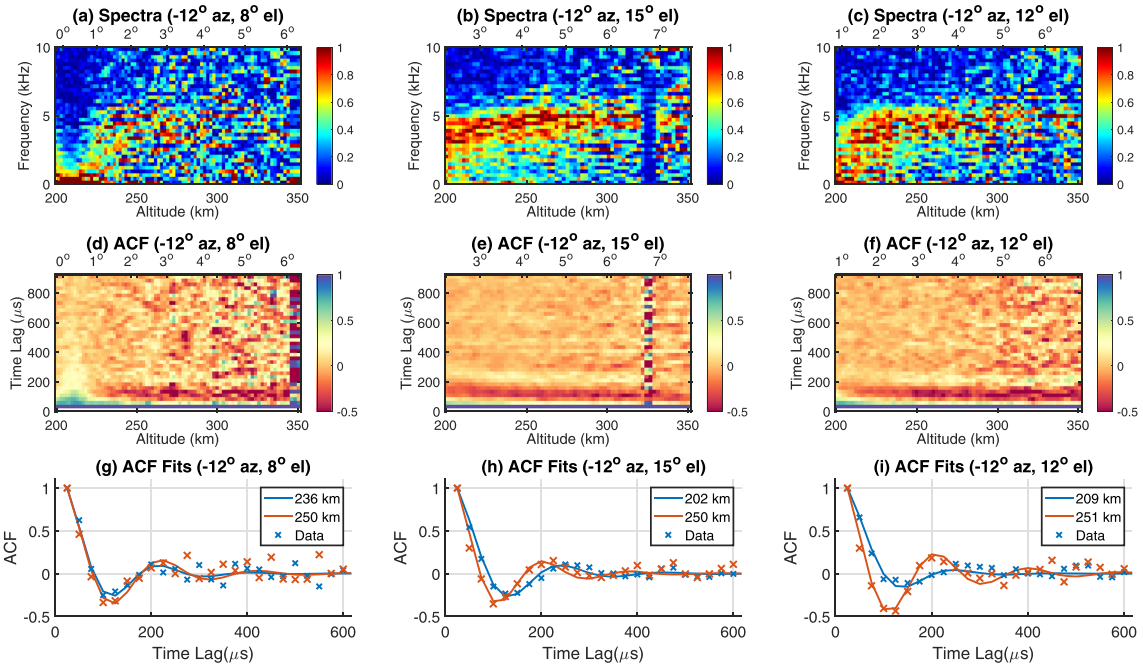

FIGURE 3. Spectrograms measured on 4 April 2019 are shown in plots (a), (b), and (c). The ACFs in plots (d), (e), and (f) are fit to the Brownian collisional model. Plots (g), (h), and (i) show selected best fits (solid colors) to the measured ACFs (x points).

Figure 4 shows the measured and fitted temperature profiles from November 2013, with a 15-km range resolution providing ~0.2° effective aspect angle resolution. The data show $T_e/T_i < 1$ fits at aspect angles of 3.6° and less and demonstrate that the Brownian theory underestimates the collisional effects at those aspect angles. Furthermore, at aspect angles of 4° to 4.6° the T_e/T_i ratio is larger than 1, but that value is well below the expected ratio calculated using the IRI climatological model (Bilitza & Reinisch, 2008; Hedin, 1991). Comparing the fitted ion and electron temperatures to the IRI predictions shows that the nonphysical T_e/T_i measurements are the result of both underestimating T_e and overestimating T_i.

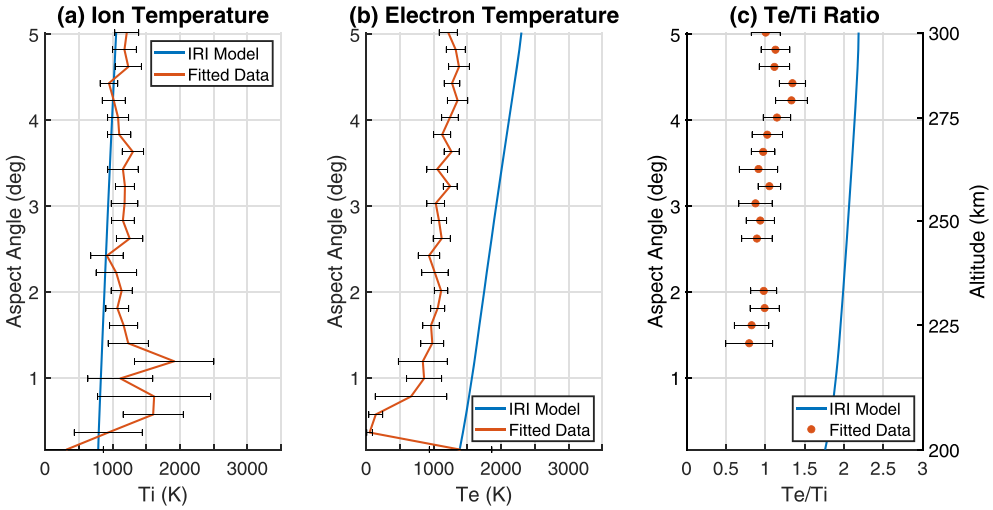

FIGURE 4. The fitted temperature (orange) to the ACFs measured on 8 November 2013. In plot (a), the ion temperatures are slightly elevated compared to the IRI model (blue), but in plot (b), the electron temperatures are much lower than IRI predicts. Plot (c) shows the T_e/T_i ratio for data points that converged on a solution with errors less than 25%.

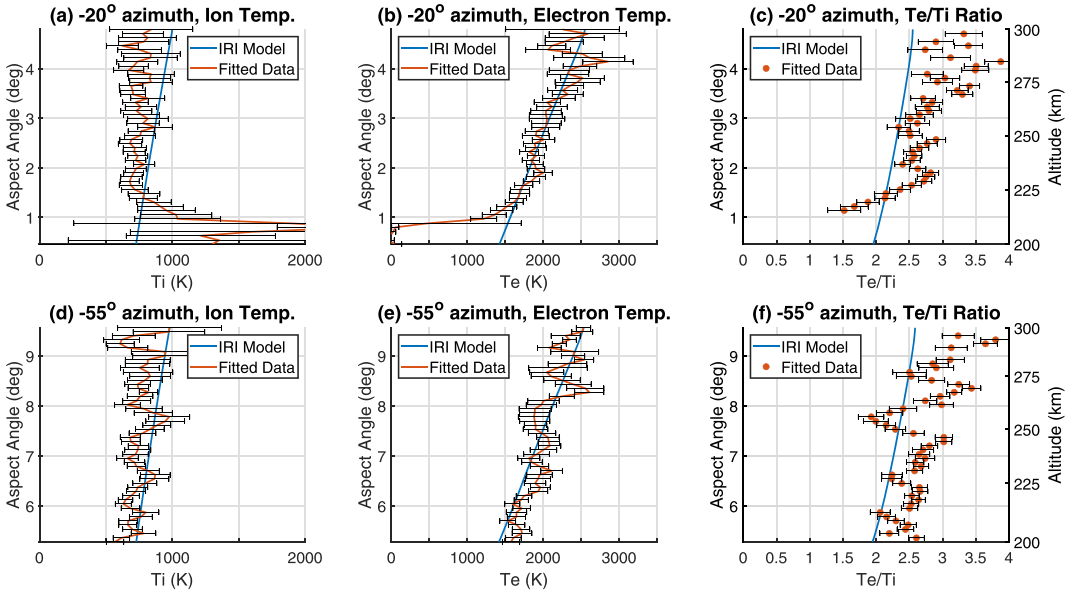

FIGURE 5. The fitted temperatures for ACFs measured on 20 February 2019. Both antenna positions show fitted ion and electron temperatures near the IRI predictions (plots a, b, d, and e). The quality fits in plots (c) and (f) show temperature ratios larger than 1 at all plotted aspect angles, which is a physically valid solution.

The fitted temperatures from the 22 February 2019 experiment with 18-km range resolution are plotted in Figure 5. For both positions, only the data from 200 to 300 km is shown to reduce complexity, as it restricts the analysis to the O^+ dominant region and altitudes with good SNR. Both the ion and electron temperatures are reasonably consistent with the IRI model predictions, especially compared to the fits in Figure 4 to the November 2013 data. Plot (c) in Figure 5 shows physically valid T_e/T_i ratios for fitted ACFs that have error bars less than 25% and exit conditions that indicate convergence to a global minimum. A sharp increase in the temperature ratio from 1.5 to 3 occurs between 1° and 2° in aspect angle, which may indicate collisions affecting the spectra near 1°, but could also be due to the previously mentioned lack of beam averaging. The temperature profiles in Figure 6 show a similar trend occurred for the 4 April 2019 experiment. The fitted electron and ion temperatures follow the IRI model well at altitudes between 200 and 300 km and therefore show physically valid and reasonable temperature ratios at aspect angles of 1.25° and above.

Both 2019 experiments unexpectedly produced physically valid temperature ratios near the IRI predictions. This is likely due to the overall lower collision rates on those days. The UMass Lowell Digisonde shows that the 2013 experiment had a peak density at 275 km of 1.5×10^{12} m^{-3}, while the peak densities in the February and April 2019 experiments were both at 200 km and 3.8×10^{11} m^{-3} and 2.5×10^{11} m^{-3}, respectively. The average Coulomb collision rate varies as

$$\nu_e \propto \frac{n_e}{T^{3/2}}, \tag{7}$$

so the collision rate for November 2013 is approximately four times higher than the collision rate in February 2019 and six times higher than the collision rate in April 2019. The Sulzer and González (1999) explanation for Coulomb collisions narrowing IS radar spectra is that as the aspect angle decreases, electrons have to move a longer distance along field lines to move one Bragg wavelength towards or away from the radar, which gives a higher chance of a collision occurring. This explanation more formally relates to the correlation time of an electron, which is how long the electron stays near its initial position. If this correlation time starts approaching the collisional timescale, $1/\nu_e$, then a collision will likely occur, which damps the ion-acoustic mode and causes the spectra to narrow.

The correlation time of an electron is

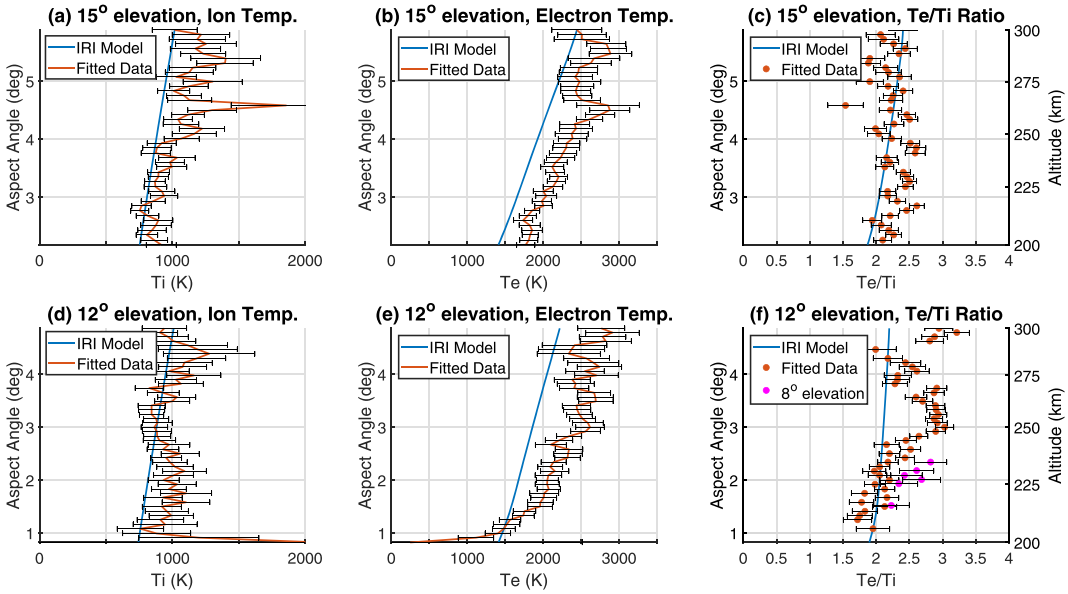

FIGURE 6. The fitted temperatures for ACFs measured on 4 April 2019. The ion and electron temperatures (plots a, b, d, and e) all follow the general trend of IRI, and the temperature ratios for data points with good fits are physically valid at all aspect angles above 1°. In plot (f), the small number of points from the 8° elevation angle position with good fits is plotted in magenta as a function of aspect angle only.

$$\tau = \frac{\lambda_B}{v_{th} \sin\alpha}, \tag{8}$$

where λ_B is the radar's Bragg scattering vector. The timescale argument from Sulzer and González (1999) is then formalized: the spectra are narrower than collisionless theory if

$$\frac{\kappa}{\nu_e} < \tau = \frac{\lambda_B}{v_{th} \sin\alpha}, \tag{9}$$

where ν_e is an averaged collision rate and κ is a scaling constant that accounts for the kinetic behavior of Coulomb collisions. Approximating the thermal speed as constant, equation 9 allows two densities to be compared to the critical aspect angle, α_c, where the spectra starts to narrow compared to collisionless theory:

$$\frac{\sin\alpha_{c1}}{n_{e1}} = \frac{\sin\alpha_{c2}}{n_{e2}}. \tag{10}$$

Figure 4 shows for the November 2013 experiment that this critical angle is around 5°. Since the peak density, and thus collision rates, in February and April 2019 are respectively four and six times lower than in November 2013, equation 10 calculates the critical aspect angles as 1.25° for February 2019 and 0.8° for April 2019. Thus, at aspect angles larger than 1.25° and 0.8° collisions should not affect the spectra on those days. This is in agreement with Figures 5 and 6, which show physically valid T_e/T_i ratios at these aspect angles, and a rapid decrease in T_e/T_i at aspect angles below 1.5° in the February 2019 data in Figure 6, though the decrease could also be due to the lack of beam averaging. The high-range resolution of the experiments reduces the need for averaging the forward model over the antenna's beam pattern, but spectra at aspect angles less than about 1° still measure the sharply peaked 0° aspect angle mode in the main lobe of the beam (see Figures 1b, 2a, and 3a). Therefore, all temperature fits at aspect angles below 1° should not be trusted without beam averaging the forward model.

4. Analysis of Measured ACFs

The ACFs measured on 8 November 2013 were fit to a Brownian collisional theory (Kudeki & Milla, 2011) and produced $T_e/T_i \leq 1$ at aspect angles less than ~5°, whereas IRI predicts $T_e/T_i \approx 2$ (Figure 4). The

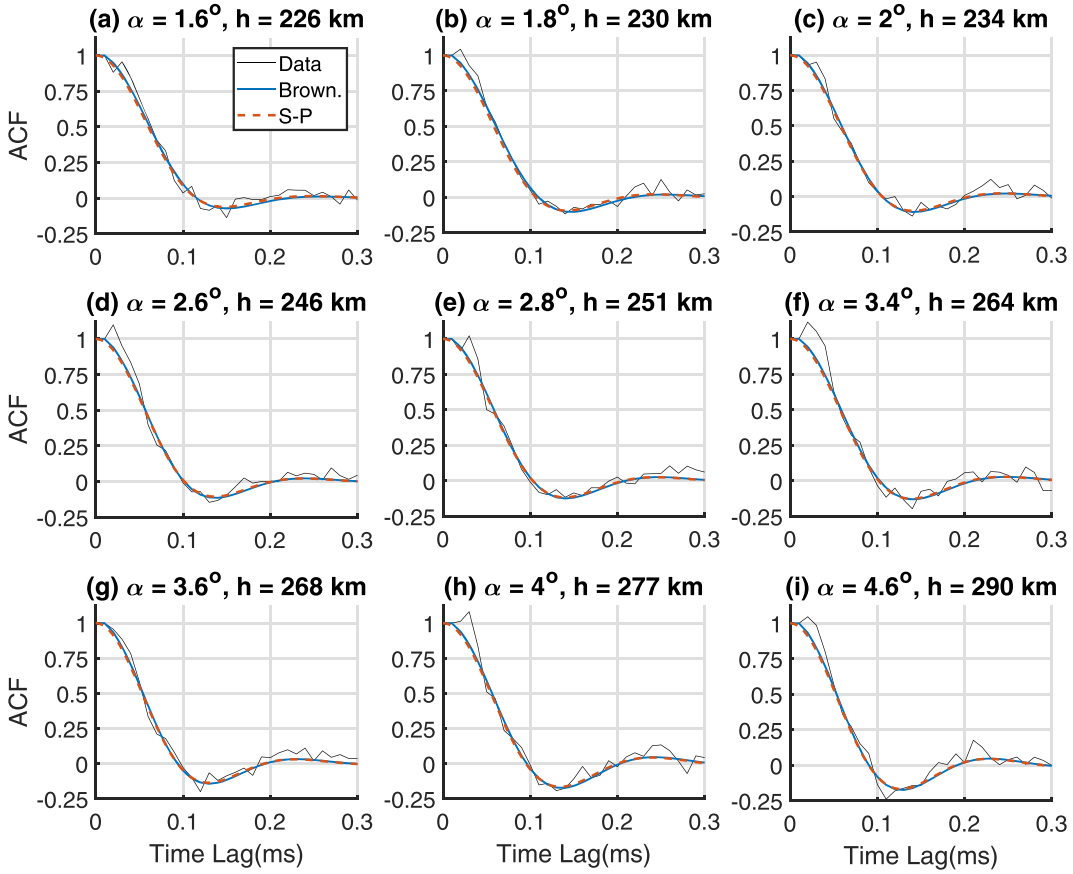

FIGURE 7. The observed ACFs (black) are compared to the Brownian theory fits (blue) and single-particle simulations (orange) that use T_e and T_i from the Brownian fits. At aspect angles of 3.4° and larger, the Brownian theory is identical to the single-particle simulations. The data and fitted ACFs are all normalized to the first nonzero time lag. The best fit temperatures are listed in Table 2.

Brownian collisional model is the most accurate analytic theory and is useful for quickly inverting measured ACFs at Millstone Hill where aspect angles less than 5° are not often measured. The Jicamarca IS radar only looks at aspect angles less than 5° due to its equatorial location and steering capabilities. As a result, Jicamarca uses the simulations from Sulzer and González (1999), which was improved upon in Milla and Kudeki (2011), as the forward model for temperature fittings. In this section, we compare the measured ACFs at Millstone Hill to the forward model from Milla and Kudeki (2011) and then compare the Milla and Kudeki (2011) forward model to the PIC simulations in Longley et al. (2018, 2019).

4.1. Comparison to Single-Particle Simulations

We will first compare the measured ACFs to the single-particle simulations from Kudeki and Milla (2011), which are an extension of the Sulzer and González (1999) model that is currently used for temperature fittings at Jicamarca (Aponte et al., 2001). Figure 7 shows the measured ACFs from 8 November 2013 at aspect angles where the Brownian theory fits the data well (see plot c in Figure 4). The temperatures that best fit the data are listed in Table 2 and are used to run the single-particle simulations with a constant density of $n = 10^{12}$ m^{-3} for each range gate. The single-particle simulations numerically calculate the electron Gordeyev integral (equation 4), which is used in the linear framework of equations 1–3 to calculate the IS spectra. The ACFs are then obtained by a Fourier transform and are plotted in Figure 7.

To more quantitatively investigate the difference between the ACFs in Figure 7, the single-particle simulations are treated as data and then fit back to the Brownian theory using the inversion process described in Section 3. The best fit temperatures of the Brownian theory to the single-particle ACFs are listed in Table 2 and have error bars of 1.5% or less on all the fits. Ideally, the single-particle simulations would be

Table 2
The Fitted Temperatures (in K) using the Brownian Theory for Several Aspect Angles From the 8 November 2013 Experiment

Altitude	226	230	234	246	251	264	268	277	290
Aspect Ang.	1.61°	1.81°	2.01°	2.62°	2.83°	3.43°	3.63°	4.03°	4.62°
Brownian Fit, T_i	1,167	1,072	1,136	1,254	1,154	1,154	1,302	1,082	1,235
Brownian Fit, T_e	955	1,056	1,107	1,115	1,076	1,050	1,262	1,239	1,377
SP Back-Fit, T_i	1,254	1,174	1,170	1,277	1,178	1,173	1,318	1,113	1,248
SP Back-Fit, T_e	923	1,079	1,082	1,081	1,059	1,062	1,246	1,240	1,364
Scaling	1.11	1.07	1.05	1.05	1.04	1.01	1.02	1.03	1.02

Note. The best fit temperatures are then used to run the single-particle simulations from Milla and Kudeki (2011). Those simulations are then fit back to the Brownian theory (labeled as SP Back-Fit) to show how the single-particle simulations will improve T_e/T_i estimates at smaller aspect angles. Equation 11 calculates the scaling factor needed for the Brownian model to calculate the same T_e/T_i as the single-particle simulations. A scaling factor close to 1 indicates both forward models will produce the same T_e/T_i estimate, and a scaling ratio larger than 1 shows that fitting the data to the single-particle model will produce larger, more physical T_e/T_i ratios than fitting to the Brownian model.

used to directly fit the data, but this is not feasible due to the computational time required to produce a single ACF. Thus, the fitting of the single-particle simulations to the Brownian theory (which provided the temperatures for the simulations) is a rough estimate of the improvement the single-particle simulations would have on fitting the data. The best metric for this improvement would be a scaling ratio for T_e/T_i, similar to the ad hoc fix used at Jicamarca before the Sulzer and González (1999) simulations (Aponte et al., 2001). This scaling measure is listed in Table 2 and is calculated as

$$\text{Scaling}=\left(\frac{T_{e,Br}}{T_{i,Br}}\right)\cdot\left(\frac{T_{i,SP}}{T_{e,SP}}\right) \tag{11}$$

This scaling ratio in Table 2 has a significant drop off towards unity between 2.83° and 3.43° in aspect angle, showing that for this experiment fitting the Brownian theory and single-particle simulations to the data would produce nearly identical temperature estimates at aspect angles of 3.4° and higher. Figure 7 and Table 2 show that the single-particle simulations at 3.43° and 3.63° have converged on the Brownian theory with a nonphysical $T_e/T_i < 1$ ratio. As shown in Section 3, this aspect angle of convergence between the two models is generally dependent on the density and collision rate.

4.2. Comparison to PIC Simulations

The PIC simulations in Longley et al. (2019) showed that nonlinear, kinetic effects from electron–electron collisions will cause a narrowing of the spectra at aspect angles as large as 5°. To compare this prediction to IS radar measurements, a set of PIC simulations is run with parameters similar to those found from the Brownian fits to the November 2013 data at 2.83° and 3.43°. The PIC code solves the electron and ion Boltzmann equations by discretizing the distribution function into macroparticles, which then evolve in time from the Lorentz force and the Fokker-Planck collision operator. Since the PIC code is solving the full nonlinear equations, the electron and ion distributions are coupled through the self-consistent electric field. This coupling tends to drive both distributions towards equilibrium, so a simulation with $T_e \neq T_i$ will slowly evolve to one with $T_e = T_i$. Properly simulating $T_e \neq T_i$ in the PIC code requires an additional collision operator that acts to heat the electron distribution, similar to photoionization, as well as including the ion-neutral collisions which keep the ion temperature lower than the electron temperature throughout the day. In contrast, the Brownian theory and single-particle simulations can calculate $T_e \neq T_i$ spectra by assuming the system is quasistationary and calculating the ACFs of each distribution separately (Kudeki & Milla, 2011). To avoid this heating-related difficulty, the PIC code is run in equilibrium with $T_e = T_i$.

The temperatures used in the PIC simulation are chosen to be $T_e = T_i = 1{,}150$ K, which is the closest equilibrium temperature to the measured ACFs at 2.83° and 3.43°. Those aspect angles correspond to altitudes above 250 km, so a 100% O^+ composition is appropriate. The grid is chosen such that the grid step $\Delta x = 0.5$ cm is significantly less than the Debye length of $\lambda_D = 1.1$ cm to avoid numerical heating (Birdsall & Langdon, 2004). Since the simulation needs to run for 20 ms to obtain 50-Hz resolution of the spectra, two artificial parameter choices are made. First, the density is lowered to 5×10^{10} m^{-3} in order to increase the Debye length and avoid numerical heating. The collision operator is still calculated with a

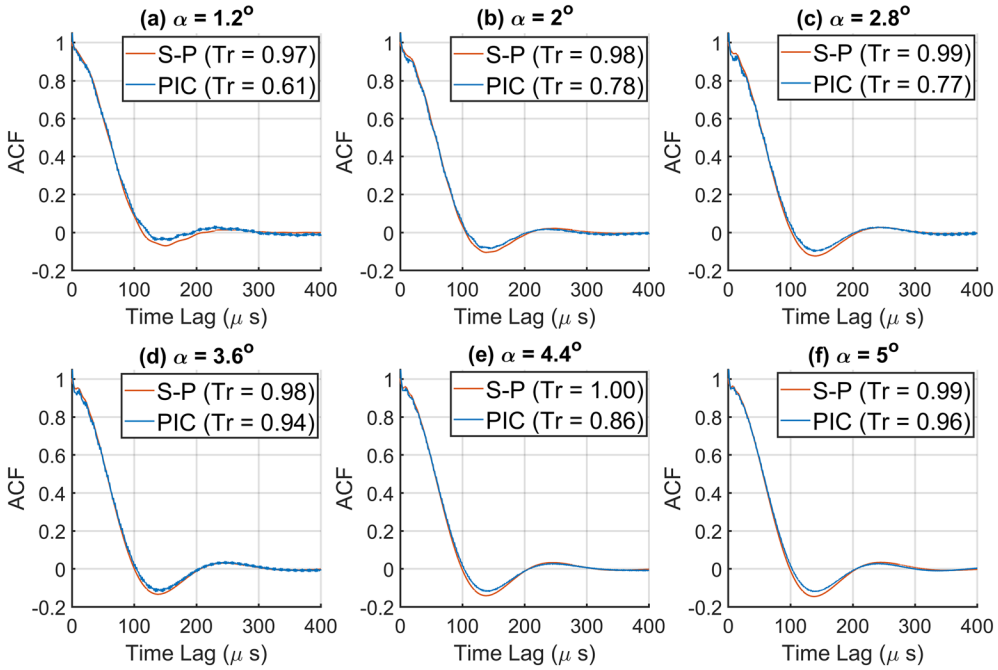

FIGURE 8. The PIC simulations (blue) and the single-particle simulations (orange) are run at different aspect angles using the same plasma parameters (including artificial electron mass and density). The temperature ratios, $T_r = T_e/T_i$, are calculated by fitting the simulated ACFs to Brownian theory using the same methods discussed in section 2.2. The errors for all the fits are less than 2%.

density of 10^{12} m^{-3} to make the simulations comparable to the data. Second, the electron mass in the simulation is set as 28.5 times heavier, which reduces the plasma frequency by a factor of $\sqrt{28.5} \approx 5.4$. The Courant condition for stability in a PIC code simplifies to $\Delta t \leq C/\omega_p$, where C is a constant specific to the problem. Thus, raising the electron mass by a factor of 28.5 reduces the runtime of the simulation by a factor of 5.4. This mass adjustment requires raising the electron gyrofrequency by a factor of 5.4 to keep the ratio ν_e/Ω_e in equation 5 constant (Longley et al., 2018; see also Diaz et al., 2008). The resulting time step is 40 ns. With these parameters and a 1,024 by 1,024 grid, the aspect angle resolution of the simulation is 0.71°. For aspect angles larger than 0.71°, the spectra can be interpolated in (k_x, k_y) space with good accuracy, but at smaller angles, this interpolation necessarily includes the exactly perpendicular to B grid point which dominates the spectra with a sharp spike at low frequencies (Longley et al., 2019). Since IS radar measurements require an averaging over many samples, the PIC code is run 100 times with different random seeds to give different initial particle positions and different random number draws during the collision algorithm.

Figure 8 shows the results of the PIC simulation at small aspect angles. The single-particle simulations are run with the same parameters as the PIC code for comparison (including artificial electron mass and density). At all of the shown aspect angles, the ACFs from the PIC code are the same width as those from the single-particle simulations, indicating that both models should reproduce the same T_i measurement. However, all of the ACFs from the PIC code have a shallower minimum around 150 μs compared to the single-particle ACFs. Since the ACF is effectively measuring a position (electron correlation across a wavelength) over time, the depth of the minimum can be interpreted as the damping strength of an oscillator. Without any damping of the ion-acoustic mode, the ACF would be a cosine function, so therefore, the shallower minimums in the PIC code ACFs indicate a more heavily damped wave than what the single-particle simulations predict. The total damping rate in the PIC code is higher than the total damping rate in the single-particle simulations due to a nonlinear feedback between the collisional and Landau damping (Longley et al., 2019). Fitting the measured ACFs from Millstone to a forward model that underestimates collisional damping would cause the fitting routine to compensate by lowering T_e/T_i, as if Landau damping were stronger in the forward model than it actually is.

To qualitatively investigate the difference between the PIC and the single-particle models, the ACFs from each simulation are run through the same fitting routine as the data were in section 3, with the Brownian theory as the forward model (also using artificial simulation parameters). The best fit temperature ratios are listed in legends in Figure 8, and for the plotted aspect angles of 1.2° to 5°, the PIC simulations are best fit by the Brownian theory with $T_e/T_i < 1$. In contrast, the best fit temperatures to the single-particle simulations all produce $T_e/T_i > 0.97$, indicating that the single-particle simulations are producing nearly the same ACF as the Brownian model. This convergence between the single-particle simulations and the Brownian model is also seen in Figure 7 and Table 2, where the Brownian theory and single-particle simulations produce nearly identical temperature estimates at aspect angles of 3.4° and larger.

5. Discussion

In this paper, the ACFs measured by a 440-MHz radar were fit to collisional IS radar theory and then compared to ACFs from single-particle and PIC simulations. The comparison of 440-MHz ACFs to collisional forward models clearly demonstrates that the importance of Coulomb collisions depends both on the aspect angle and on the collision rate—which is controlled by the plasma density and temperature. The experiment on 8 November 2013 was near solar maximum, with an average 10.7 cm (F10.7) value of 150 solar flux units (SFU; 10^{-22} W/m^2/Hz) producing a peak density of 1.5×10^{12} m^{-3} in the F_2 region. The measured ACFs show that Coulomb collisions are responsible for $T_e/T_i < 1$ fits at aspect angles of 3.6° and below when fitting to a Brownian collisional theory. The ACFs at 4° and 4.6° also look collisionally narrowed, but the fitting routine obtained a physically valid $T_e/T_i > 1$ ratio. The experiments in February and April 2019 took place closer to solar minimum where the average F10.7 was 70 SFU, and the peak densities of 3.8×10^{11} m^{-3} and 2.5×10^{11} m^{-3} occurred at lower altitudes. The lower densities dropped the collision rates, and the spectra observed by Millstone Hill produced best fit results with no significant drop in T_e/T_i compared to the IRI model at aspect angles above 1.5°. Below 1° aspect angle, averaging the forward model over the beam pattern becomes necessary and this was not done in this study, so we were thus not able to definitively see if equation 10 correctly predicts that collisional effects become important at 1.25° and 0.8° for the February and April measurements respectively.

The ACFs measured at Millstone Hill on 8 November 2013 were further compared to the single-particle simulations from Milla and Kudeki (2011) and indirectly to the PIC simulations from Longley et al. (2019) to investigate the validity of those two models. At aspect angles of 3.4° and larger, the single-particle simulations were nearly identical to the Brownian theory for the same temperatures. This means using the single-particle simulations as the forward model in the fitting process would still reproduce the $T_e/T_i < 1$ fits to the November 2013 data at 3.4° and 3.6°. Comparing the single-particle simulations to PIC simulations with fixed $T_e = T_i = 1{,}150$ K showed that at all aspect angles less than 5°, the PIC simulations produce more heavily damped ACFs than the single-particle simulations. This suggests that using the PIC simulations as a forward model in the fitting routine would lead to more accurate T_e/T_i ratios for the data measured on 8 November 2013 but not for the measurements in February and April 2019 where the density remained low.

Lastly, the results from the February and April 2019 experiments are in slight contrast with earlier studies by Aponte et al. (2001) but can be reconciled by examining scattering theory parameter dependence. In particular, the data set analyzed by Aponte was taken at the equatorially located 50-MHz Jicamarca radar. At aspect angles of 3.5° and less, and for a wide range of densities and temperatures, they found that collisions narrowed the spectra and produced nonphysical T_e/T_i ratios. Furthermore, fitting the spectra to the single-particle simulations from Sulzer and González (1999) showed that all of the T_e/T_i ratios were being underestimated at aspect angles of 3.5° or less and could be corrected to $T_e/T_i \geq 1$ with the single-particle simulations. This higher sensitivity to collisions even at low densities can be explained due to the lower transmission frequency of Jicamarca. The Bragg scattering wavelength of 3 m at Jicamarca is about nine times longer than the 0.34-cm Bragg wavelength of Millstone Hill, so according to equation 8, the electron correlation time is nine times longer at Jicamarca. Therefore, when the density drops by a factor of 5, as it did for the February and April 2019 Millstone Hill experiments, a hypothetical experiment at the Jicamarca radar wavelength would still see collisional effects at a wider range of aspect angles since the correlation time is nine times longer than at Millstone Hill. This implies that one would expect to always see collisions affecting T_e/T_i measurements at intermediate aspect angles with VHF IS radars similar to

Jicamarca. By contrast, Millstone Hill at UHF frequencies is only affected for the same intermediate aspect angle range when the density is high (~10^{12} m^{-3}). This can occur frequently at Millstone Hill during solar maximum, as the 8 November 2013 experiment showed, or during an extreme storm time event where densities are increased due to particle precipitation, electron heating, or heavy O+ mass transport. The latter occurs within storm-enhanced density plumes which frequently occur in the storm time dusk sector subauroral ionosphere (Foster et al., 2002).

Acknowledgments
This work was supported by National Aeronautics and Space Administration (NASA) grants NNX14AI13G and NNX16AB80G and National Science Foundation (NSF) grants PHY-1500439 and AGS-1755350. This work used the XSEDE and TACC computational facilities, supported by NSF grant ACI-1053575. Radar observations and analysis at Millstone Hill and the Madrigal distributed database system are supported by NSF Cooperative Agreement AGS-1762141 with the Massachusetts Institute of Technology. PIC simulation and single-particle simulation produced data are available on Zenodo at doi:10.5281/zenodo.3565938. EPPIC is available at gitlab.com/oppenheim_public, and the code version used in this paper is archived at doi:10.5281/zenodo.3565938. The IRI model results have been provided by the Community Coordinated Modeling Center at Goddard Space Flight Center through their public Runs on Request system (http://ccmc.gsfc.nasa.gov). The IRI Model was developed by Dieter Bilitza at the NASA Goddard Space Flight Center. More detail can be found in the Ph.D. thesis of William Longley (https://library.bu.edu/theses), upon which this paper is based.

References

Aponte, N., Sulzer, M. P., & González, S. A. (2001). Correction of the Jicamarca electron-ion temperature ratio problem: Verifying the effect of electron Coulomb collisions on the incoherent scatter spectrum. *Journal of Geophysical Research*, *106*(A11), 24,785–24,793. https://doi.org/10.1029/2001JA000103

Beynon, W. J. G., & Williams, P. J. S. (1978). Incoherent scatter of radio waves from the ionosphere. *Reports on Progress in Physics*, *41*(6), 909–955. https://doi.org/10.1088/0034-4885/41/6/003

Bilitza, D., & Reinisch, B. W. (2008). International Reference Ionosphere 2007: Improvements and new parameters. *Journal of Advances in Space Research*, *42*(4). https://doi.org/10.1016/j.asr.2007.07.048

Birdsall, C. K., & Langdon, A. B. (2004). *Plasma physics via computer simulation*. Boca Raton: CRC Press.

Diaz, M. A., Semeter, J. L., Oppenheim, M., & Zettergren, M. (2008). Particle-in-cell simulation of the incoherent scatter radar spectrum. *Radio Science*, *43*, RS1007. https://doi.org/10.1029/2007RS003722

Erickson, P. J., MIT/Haystack Observatory. (2013) Data from the CEDAR Madrigal database. Available from https://w3id.org/cedar?experiment_list=experiments/2013/mlh/08nov13&file_list=mlh_spec2013_11_08.001.hdf5

Erickson, P. J., MIT/Haystack Observatory. (2019a) Data from the CEDAR Madrigal database. Available from https://w3id.org/cedar?experiment_list=experiments/2019/mlh/22feb19&file_list=mlh_spec2019_02_22.001.hdf5

Erickson, P. J., MIT/Haystack Observatory. (2019b) Data from the CEDAR Madrigal database. Available from https://w3id.org/cedar?experiment_list=experiments/2019/mlh/04apr19&file_list=mlh_spec2019_04_04.001.hdf5

Evans, J. V. (1972). Ionospheric movements measured by incoherent scatter: A review. *Journal of Atmospheric and Solar - Terrestrial Physics*, *34*(2), 175–209. https://doi.org/10.1016/0021-9169(72)90164-X

Foster, J. C., Erickson, P. J., Coster, A. J., Goldstein, J., & Rich, F. J. (2002). Ionospheric signatures of plasmaspheric tails. *Geophysical Research Letters*, *29*(13), 1623. https://doi.org/10.1029/2002GL015067

Froula, D. H., Glenzer, S. H., Luhmann, N. C. Jr., & Sheffield, J. (2011). *Plasma scattering of electromagnetic radiation: Theory and measurement techniques*. Burlington, MA: Academic Press. https://doi.org/10.1016/B978-0-12-374877-5.00001-4

Gordeyev, G. V. (1952). Plasma oscillations in a magnetic field. *Soviet Physics - JETP*, *6*, 660–669.

Gordon, W. E. (1958). Incoherent scattering of radio waves by free electrons with applications to space exploration by radar. *Proceedings of the IRE*, *46*(11), 1824–1829. https://doi.org/10.1109/JRPROC.1958.286852

Hedin, A. E. (1991). Extension of the MSIS thermosphere model into the middle and lower atmosphere. *Journal of Geophysical Research*, *96*(A2), 1159–1172. https://doi.org/10.1029/90JA02125

Hysell, D. L., Milla, M. A., Condori, L., & Vierinen, J. (2015). Data-driven numerical simulations of equatorial spread F in the Peruvian sector 3: Solstice. *Journal of Geophysical Research: Space Physics*, *120*, 809–10,822. https://doi.org/10.1002/2015JA021877

Kubo, R. (1966). The fluctuation-dissipation theorem. *Reports on Progress in Physics*, *29*(1), 255. https://doi.org/10.1088/0034-4885/29/1/306

Kudeki, E., & Milla, M. (2011). Incoherent scatter spectral theories part I: A general framework and results for small magnetic aspect angles. *IEEE Transactions on Geoscience and Remote Sensing*, *49*(1), 315–328. https://doi.org/10.1109/TGRS.2010.2057252

Lehtinen, M. S., & Häggström, I. (1987). A new modulation principle for incoherent scatter measurements. *Radio Science*, *22*(4), 625–634. https://doi.org/10.1029/RS022i004p00625

Lehtinen, M. S., & Huuskonen, A. (1996). General incoherent scatter analysis and GUISDAP. *Journal of Atmospheric and Solar - Terrestrial Physics*, *58*, 435. https://doi.org/10.1016/0021-9169(95)00047-X

Longley, W. J., Oppenheim, M. M., Fletcher, A. C., & Dimant, Y. S. (2018). ISR spectra simulations with electron-ion Coulomb collisions. *Journal of Geophysical Research: Space Physics*, *123*, 2990–3004. https://doi.org/10.1002/2017JA025015

Longley, W. J., Oppenheim, M. M., & Dimant, Y. S. (2019). Nonlinear effects of electron-electron collisions on ISR temperature measurements. *Journal of Geophysical Research: Space Physics*, *124*, 6313–6329. https://doi.org/10.1002/2019JA026753

Milla, M., & Kudeki, E. (2011). Incoherent scatter spectral theories part II: Modeling the spectrum for modes propagating perpendicular to B. *IEEE Transactions on Geoscience and Remote Sensing*, *49*(1), 329–345. https://doi.org/10.1109/TGRS.2010.2057253

Sulzer, M. P. (1986). A radar technique for high range resolution incoherent scatter autocorrelation function measurements utilizing the full average power of klystron radars. *Radio Science*, *21*(6), 1033–1040. https://doi.org/10.1029/RS021i006p01033

Sulzer, M. P., & González, S. (1999). The effect of electron Coulomb collisions on the incoherent scatter spectrum in the F region at Jicamarca. *Journal of Geophysical Research*, *104*(A10), 22,535–22,551. https://doi.org/10.1029/1999JA900288

Virtanen, I. I., Lehtinen, M. S., Nygrén, T., Orispää, M., & Vierinen, J. (2008). Lag profile inversion method for EISCAT data analysis. *Annales de Geophysique*, *26*(571–581), 2008. https://doi.org/10.5194/angeo-26-571-2008

Woodman, R. F. (1967), Incoherent scattering of electromagnetic waves by a plasma, Ph.D. dissertation, Harvard Univ., Cambridge, MA, Mar. 1967.

Woodman, R. F. (2004). On a proper electron collision frequency for a Fokker-Planck collision model with Jicamarca applications. *Journal of Atmospheric and Solar - Terrestrial Physics*, *66*(17), 1521–1541. https://doi.org/10.1016/j.jastp.2004.07.001